Geophysical Journal International

Geophys. J. Int. (2025) **242,** 1–14
Advance Access publication 2025 June 09
Research Paper

https://doi.org/10.1093/gji/ggaf205

The influence of stress release on the spatial and magnitude distribution of subsequent earthquakes

Giuseppe Petrillo,[1] Eugenio Lippiello,[2] Jiancang Zhuang[3] and Warner Marzocchi[4]

[1] *Earth Observatory of Singapore—Nanyang Technological University (NTU), Nanyang Ave, Block N2-01a-15,* 639798*, Singapore*
[2] *Department of Mathematics and Physics, University of Campania "L. Vanvitelli", Viale Lincoln* 5, I-81100 *Caserta, Italy*
[3] *The Institute of Statistical Mathematics, Research Organization of Information and Systems,* 190-0014*, Tokyo, Japan*
[4] *Department of Earth, Environmental, and Resources Sciences, The University of Naples Federico II, Via Cinthia,* 21–80126*, Naples, Italy.*
E-mail: warner.marzocchi@unina.it

Accepted 2025 May 29. Received 2025 April 16; in original form 2024 December 9

SUMMARY

Determining when and where the next big earthquake will occur is a fundamental challenge in earthquake forecasting. Although it is reasonable to assume that the next major earthquake will occur in regions where stress has been increased by previous events, the most common and reliable earthquake forecasting models assume that the magnitude of next earthquakes is independent from what happen before and, implicitly, from the stress state. In this study, we investigate the correlation between stress distribution and the occurrence of large earthquakes using a realistic physical model. Our findings reveal that the next big earthquake is more likely to occur on the periphery of previous large earthquakes, where stress has accumulated but not yet been relaxed. Additionally, we explore how stress redistribution influences the magnitude distribution of aftershocks. These results can inform the introduction of correlations between large earthquakes in existing seismic forecasting models, potentially enhancing their accuracy and reliability.

Key words: Numerical modelling; Persistence, memory, correlations, clustering; Self-organization; Spatial analysis; Statistical methods; Statistical Seismology.

1 INTRODUCTION

It is reasonable to assume that earthquakes occur with higher probabilities in regions where and when the stress level is higher. However, in most situations, there is significant uncertainty in identifying regions of increased stress. This uncertainty arises from various factors, including the complexity of fault geometry and variability in fault slip behaviour. For instance, the 2021 Maduo earthquake study highlights the influence of varying dip angles and fault geometries on rupture propagation and earthquake dynamics (Wei *et al.* 2023). Similarly, the analysis of the 2022 Luding earthquake demonstrates how interactions with surrounding fault segments and asperities can significantly affect stress distribution (Li *et al.* 2022). Additionally, methods to estimate uncertainty in coseismic slip distributions often involve sophisticated statistical techniques, such as Bayesian source inversion, to combine observational data with prior model information, but these estimations are unavoidably untestable directly with observations. All of these issues pose challenges for accurately identifying regions characterized by increase of stress (Duputel *et al.* 2014). Furthermore, real-time applications, like tsunami inundation forecasting based on coseismic slip models, demonstrate that even with advanced algorithms and high-resolution data, there is a need for multiple models to account for the variability and uncertainty in slip distributions. This approach underscores the difficulty in pinpointing precise areas of increased stress due to the inherent uncertainties in the models (Ohno *et al.* 2022).

Therefore, it remains a significant challenge to determine whether the stress redistributed by a main shock increases the probability of a subsequent large main shock occurring in areas where stress has been heightened. This question is central to understanding where and when the next big earthquake is likely to occur.

In the face of the impossibility of providing a definite answer to this question, the most widely used statistical models for seismic forecasting assume that the magnitude of the next main shock does not depend on the past. In other words, it occurs with equal probability at different points along a fault, independent of previous stress history. The Epidemic-Type Aftershock Sequence (ETAS) model is a prime example of this approach. Since its inception (Ogata 1988), the ETAS model has significantly improved forecasting performance and the description of earthquake clusters (Helmstetter & Sornette 2003; Console *et al.* 2010; Lombardi & Marzocchi 2010; Zhuang 2012; Spassiani *et al.* 2024). It describes earthquake occurrence as a branching process where independent earthquakes, known as background earthquakes, initiate earthquake sequences.

Each earthquake in these sequences can trigger its own aftershocks, which are localized close in time and space to the initial event. In its usual formulation, the ETAS model assumes that background earthquakes follow a time-independent Poisson process and the space distribution of historical earthquake and faults location. The most interesting aspect in terms of earthquake predictability is that the magnitude of triggered and background earthquakes has the same statistical distribution and it is independent from the state of stress and past history. This leads to the illogical consequence that the next large earthquake is more likely nucleating exactly where the previous large earthquake has just nucleated. This assumption is clearly incoherent, because it does not account for the significant change in the stress state and in the elastic energy available. Although some empirical evidence dispute the validity of such assumption (van der Elst & Shaw 2015; Stallone & Marzocchi 2019), a physical explanation is still lacking.

This scenario is consistent with the observations (Schoenberg & Bolt 2000; Petrillo *et al.* 2024) that incorporating simple stress release information can improve retrospective forecasting, reflecting a non-Poissonian background occurrence rate. However, these analyses often suffer from biases in parameter estimation. An incorrect description of the laws governing aftershock triggering can lead to an inaccurate estimate of the background rate. While advancements have mitigated these issues (Petrillo & Lippiello 2021, 2023; Ross 2021; Zheng *et al.* 2021; Ross & Kolev 2022; Petrillo & Zhuang 2024), significant uncertainty remains in accurately estimating the background rate.

Given the great difficulty in tracking the evolution of stress in relay systems, earthquake simulators provide useful support. An earthquake simulator is a physical model for the evolution of stress on a seismic fault, allowing the simulation of earthquake sequences in a fault network (Nakanishi 1992; Hainzl *et al.* 1999; Mori & Kawamura 2008; Jagla *et al.* 2014; Petrillo *et al.* 2020). These models provide an important framework for interpreting the geological and mechanical behaviours that lead to seismic events. They often offer insights into stress interactions and fault dynamics that statistical models alone cannot capture.

In this study, we explore the influence of stress redistribution on the location of the subsequent large main shock by considering the two-layer fault model developed by (Petrillo *et al.* 2020). The model integrates the interactions between brittle and ductile layers within a fault zone (Perfettini & Avouac 2004; Lippiello *et al.* 2019, 2021). This model accurately capture real features of seismic occurrences, such as the Gutenberg-Richter law with a b-value consistent with instrumental findings, the occurrence of aftershocks that obey Omori's law and productivity laws similar to those in instrumental seismic sequences. Its advantage lies in the possibility to explore its long-term behaviour, well beyond the time frame covered by data. The model is intentionally simple: when the goal of a model is to aid scientists in understanding the process being studied, it is clear that a more complex model can be harder to interpret. This complexity makes it challenging to identify which physical parameters of the simulator are most crucial for accurately describing specific features of interest inside the earthquake catalogue. Hence, although being a simple model, it allows us to have total control over the slip model and the evolution of stress on the fault, which is one of the main target of this analysis. An accurate analysis by Petrillo *et al.* (2022) has shown that regions with higher stress are more prone to host subsequent large earthquakes. However, the model also indicates that precise timing information for the next large earthquake based on stress levels is not feasible.

This study presents a detailed analysis of the evolution of seismicity along a simulated seismic fault to investigate the correlation between the stress released by an earthquake and the occurrence of the subsequent large shock. Additionally, we address other fundamental questions, such as whether stress redistribution affects the size of subsequent aftershocks and if certain patterns can distinguish foreshocks from aftershocks.

Our findings have important implications for enhancing earthquake forecasting models and refining risk assessment strategies. The article is structured as follows: Section 1 describes the theoretical framework and computational setup of our two-layer fault model. Section 2 introduces relevant quantities useful for our study. Section 5 discusses the results, emphasizing their implications for earthquake forecasting and risk mitigation. The last section concludes with a summary of our contributions and perspectives on future research directions.

2 THE MODEL

3 BACKGROUND ON CELLULAR AUTOMATON MODELS

Burridge and Knopoff (BK) were the first to propose a physical model for earthquake fault dynamics (Burridge & Knopoff 1967), conceptualizing the fault as two layers in frictional contact and subject to differential driving stress, for instance due to large-scale tectonic deformation. When the local shear stress exceeds the frictional resistance, a sudden slip occurs—corresponding to an earthquake. Following the slip, the stress drops below the frictional threshold, and the system returns to a stable state until the external stress builds up again, potentially triggering subsequent events. In 1989, Bak and Tang (Bak & Tang 1989) highlighted the similarity between stick-slip dynamics in seismic activity and the behaviour of simple cellular automata, introducing the idea of self-organized criticality (SOC). Building on this, Olami, Feder and Christensen (OFC) (Olami *et al.* 1992) showed that the BK model can be mapped onto a cellular automaton model where evolution is entirely governed by local forces. In the OFC model, stress accumulates at discrete sites until a failure threshold is reached, at which point stress is redistributed to neighbouring sites, possibly triggering avalanches of varying sizes. This mechanism leads to emergent SOC behaviour, with earthquake size distributions following a power law in agreement with the Gutenberg–Richter (GR) law. However, in the broader context of applying SOC models to real seismicity, power-law size distributions are only one facet of the complex space–time–energy organization seen in natural earthquake catalogues. In particular, aftershock sequences—which follow well-known empirical relations such as the Omori law and the productivity law—represent a fundamental and arguably more distinctive feature of seismicity than the GR law alone. Classical SOC models like OFC fail to reproduce these temporal correlations, largely due to the absence of long-term memory and stress relaxation mechanisms.

In recent years, a new class of SOC models has been introduced to address this gap. These models incorporate relaxation dynamics into SOC frameworks and successfully capture several key statistical properties of real seismicity beyond simple scale invariance (Jagla 2010, 2011, 2013, 2014; Jagla & Kolton 2010; Landes *et al.* 2015; Lippiello *et al.* 2015; Landes & Lippiello 2016; Petrillo *et al.* 2020). One particularly promising direction involves generalizing the OFC model by including stress relaxation, resulting in what are known

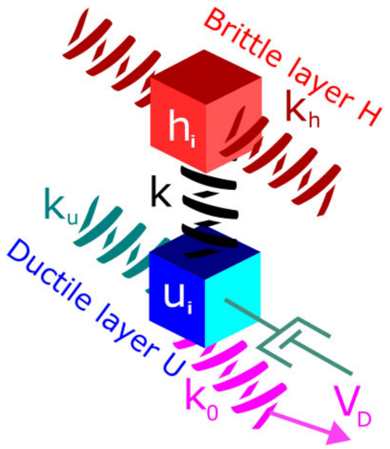

Figure 1. Schematic of the model (1-D cross-section; the other direction extends into the plane). The fault plane H is a 2-D layer with velocity-weakening friction, represented by randomly placed pinning points. The ductile region U has velocity-strengthening friction and is pulled at a constant velocity V_D. Within U, viscoelastic interactions follow a Maxwell model with dashpots and elasticity k_u. The two layers are elastically coupled with stiffness k.

as OFC with relaxation (OFCR) models. These models reproduce several features of real seismic catalogues, including spatial and temporal clustering, as well as realistic magnitude distributions.

The model considered in this study—schematically illustrated in Fig. 1 and first introduced in Petrillo *et al.* (2020)—belongs to this OFCR class. It represents the fault as a two-layer system: an upper brittle layer H and a lower ductile layer U, mimicking the brittle–ductile transition zone commonly observed in Earth's crust. This interface plays a key role in governing how stress is accumulated and released during seismic events.

This model is a variant of the original OFC model, incorporating two crucial modifications:

- Heterogeneous stress thresholds—In the classical OFC model, all sites share a uniform failure threshold. In contrast, our model assigns each site a threshold drawn from a Gaussian distribution with standard deviation σ. These thresholds are refreshed each time a site slips, introducing spatial and temporal variability.
- Stress relaxation via coupling with a ductile layer—We introduce an additional mechanism that simulates afterslip by coupling the brittle layer to an underlying ductile medium. This interaction leads to stress relaxation over an intermediate timescale and is governed by a parameter Θ.

Thus, the model is controlled by just two parameters: the disorder amplitude σ and the relaxation strength Θ. Remarkably, when both parameters are set to zero, the model reduces exactly to the original OFC model. For $\sigma > 0$ and $\Theta = 0$, the model exhibits critical behaviour belonging to the universality class of interface depinning. When both $\sigma > 0$ and $\Theta > 0$, the model defines a distinct universality class. This latter regime is of particular interest. The synthetic earthquake catalogues produced in this setting reproduce the Gutenberg–Richter law with a realistic b-value close to 1, robustly maintained across a wide range of σ and Θ. Moreover, the model naturally generates temporal clustering of events as a consequence of afterslip dynamics. These clusters follow the Omori and productivity laws with high fidelity, capturing essential features of real seismic activity.

3.1 Model structure and dynamics

Layer U, the ductile region, is subject to slow tectonic forces, moving at a constant velocity V_D. It is elastically coupled to the brittle layer H allowing stress to transfer between layers, which enables this model to capture realistic patterns of stress build-up and release. Each layer consists of a set of blocks configured on a lattice sized $L_x \times L_y$, where movement is confined to the direction of V_D. The blocks within each layer experience scalar displacements, denoted $h_i(t)$ for layer H and $u_i(t)$ for layer U. These blocks are connected elastically only to their immediate neighbours. The total stress on a block at position i in layer H is the sum of intralayer stress $f_i = k_h \Delta h_i$ and interlayer stress $g_i = k(u_i - h_i)$, where Δ represents the discretized Laplacian, and k_h and k are the elastic constants for intralayer and interlayer interactions, respectively.

3.2 Frictional behaviour and failure criteria

The friction force at layer H adheres to the Coulomb failure criterion; it becomes unstable and slips by a fixed amount Δh once the combined force $f_i + g_i$ surpasses the local friction threshold f_i^{th}. Conversely, layer U follows a velocity-strengthening friction model that adheres to the stationary form of the rate-and-state friction laws. A slip in h_i causes a corresponding coseismic slip in u_i by $q_0 \Delta h$ and in its neighbouring blocks u_j by $q_1 \Delta h$, where j are the nearest neighbours of i. When the total stress on block i in layer H exceeds f_i^{th}, the stress updates are governed by the equations:

$$\begin{aligned}
&f_i \to f_i - 4k_h \Delta h \\
&f_i \to f_j + k_h \Delta h \\
&g_i \to g_i - 4k_h \Theta \Delta h \\
&g_j \to g_j + k_h(\Theta - \epsilon)\Delta h, \qquad (1)
\end{aligned}$$

where $\Theta = (1 - q_0)\frac{k}{4k_h}$ and $\epsilon = (1 - q_0 - q_1)\frac{k}{4k_h}$.

3.3 Model phases: interseismic, coseismic and post-seismic

The model dynamics evolve through three phases:

- Interseismic phase: Stress gradually accumulates due to the slow tectonic movement of U, building up on the blocks in H.
- Coseismic phase: When the accumulated stress exceeds the frictional threshold, blocks in H slip, releasing stress abruptly in a rapid event akin to an earthquake. This phase is characterized by high-speed stress redistribution.
- Post-seismic phase: After the main slip event, stress gradually dissipates in layer U through slow afterslip, triggering aftershocks according to the Omori-Utsu decay law.

This detailed dynamic framework allows us to simulate the sequence of earthquake occurrences and their interactions effectively. To account for the natural heterogeneity of fault systems, the model does not assume initially a uniform failure threshold or strength.

3.4 Model parameters

The model behaviour is largely universal with respect to parameter choices, provided that the coupling strength θ and friction heterogeneity σ are both greater than zero. These parameters control the interaction between the brittle and ductile layers and the variability of the frictional thresholds, respectively. The role of these parameters becomes evident when considering their limiting cases:

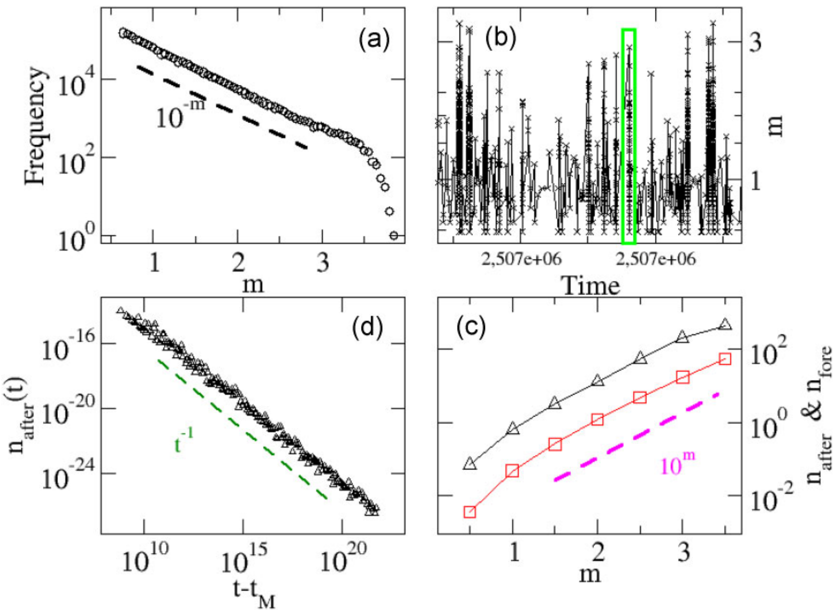

Figure 2. The main features of the earthquake simulator. (a) The Gutenberg–Richter (GR) Law, with an exponent $b = 1$, together with the numerical catalogue (b). In the green rectangle is highlighted the presence of an earthquake sequence. (c) The productivity law for the aftershocks (black triangle) which controls the number of aftershock n_{aft} as function of the main shock magnitude, m, $naft \sim 10^{\alpha m}$ with the best fit $\alpha = 1$. In the panels (d) the Omori Law. Here $p = 1$ for the temporal decay $n_{aft} \sim t^{-p}$. All the exponents are in agreement with the experimental data.

• When $\theta = 0$, the two layers are completely decoupled, and the system reduces to an OFC model with disorder, often referred to as OFC* in the literature. This corresponds to a scenario where the ductile layer does not influence seismicity, and stress redistribution occurs solely within the brittle layer.

• When $\sigma = 0$, the frictional thresholds become homogeneous, eliminating disorder in the system. In this case, the model reduces exactly to the classical OFC model with uniform stress redistribution.

For the simulations presented in this study, we set $\theta = 0.5$ and $\sigma = 5.0$, which ensures a realistic interplay between stress accumulation, redistribution and aftershock triggering. Under these conditions, previous work by Petrillo *et al.* (2022) has demonstrated that regions with higher stress are more likely to host subsequent large earthquakes, reinforcing the role of stress roughening in earthquake recurrence. The dependence of seismic memory and rupture recurrence on model parameters has been also studied in Naylor & Main (2008) where is showed that intermediate dissipation levels preserve stress heterogeneities, increasing the probability of re-rupture, while low and high dissipation levels erase memory effects, reducing clustering.

While the dissipation level can, in principle, be modified in our model, we have verified that the statistical properties of the results remain unchanged across a wide range of dissipation values. However, for very low dissipation values, finite-size effects may induce synchronization, leading the system towards a more deterministic regime. To avoid this, we have ensured that our parameter choices do not place the system in such a limit, preserving the stochastic nature of seismicity.

3.5 General results

The model proposed in Petrillo *et al.* (2020) effectively integrates a velocity-weakening elastic layer with a velocity-strengthening viscoelastic layer, capturing crucial features of seismicity. The results show that the model replicates the Gutenberg–Richter (GR) law, displaying a b-value consistent with instrumental findings. It also successfully reproduces Omori law (Utsu *et al.* 1995), depicting the decay rate of aftershock activity over time, and the productivity law, which relates the main shock magnitude to the total number of aftershocks. An overview of the results is shown in Fig. 2. To obtain these results, an initial burn-in period was applied to ensure that the system reached stationarity, as discussed in Appendix A1. Additionally, the spatial redistribution of stress before and after main shocks has been analysed to quantify stress drops and localization effects, as detailed in Appendix A2.

4 OBSERVABLES

The earthquake simulator allows for the precise definition of an earthquake sequence (see green rectangle in Fig. 2). Indeed, the simulator separates three distinct timescales, enabling the exact identification of coseismic, afterslip and interseismic phases. In our simulator, the interseismic period evolves on the slowest timescale, ensuring that a new seismic sequence begins only after the previous one has fully completed. Specifically, during an ongoing sequence, the tectonic drive is halted, meaning that interseismic loading does not progress while the system undergoes a cascade of seismic events followed by afterslip. Once the sequence is fully completed, marked by the end of afterslip, the tectonic drive resumes, initiating stress accumulation for the next sequence. During a rupture cascade, time is effectively frozen, as the rupture propagation occurs on a much shorter timescale compared to afterslip. Afterslip, in contrast, evolves on a slower timescale, during which time increases continuously. The green box in Fig. 2 thus represents the entire duration of a seismic sequence, from the onset of rupture to the completion of afterslip, marking the end of stress relaxation before a new interseismic period begins. This mechanism inherently prevents overlap between seismic sequences, unlike ETAS-like models (Touati *et al.* 2009) where overlapping sequences can occur. We define a main

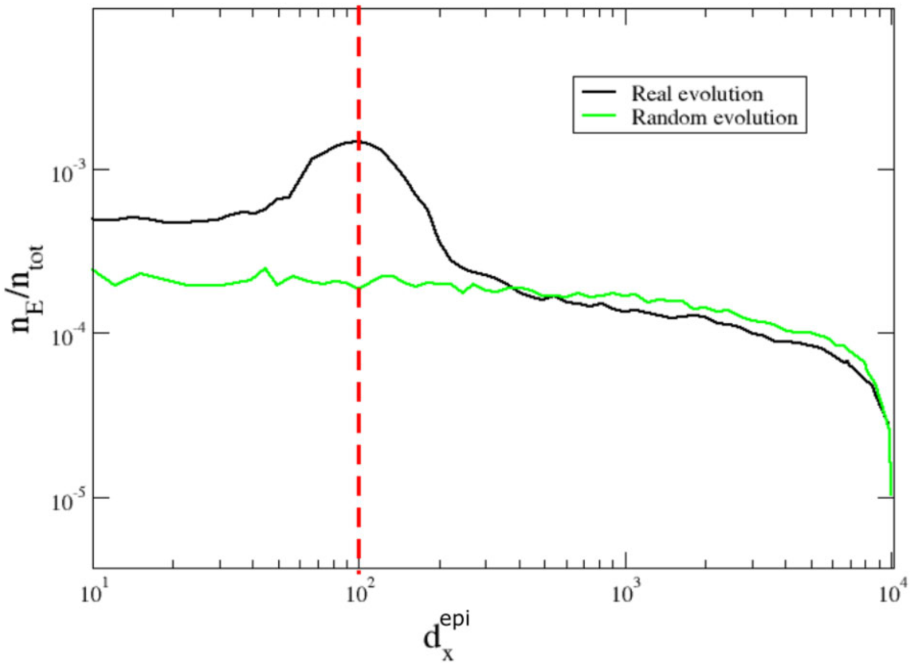

Figure 3. The ratio of subsequent main shocks as a function of the 1-D epicentral distance d_x^{epi}. The black curve represents the outcomes from the OFCR model simulations, the green curve depicts a random distribution of epicentres and the vertical dashed line indicates the characteristic horizontal extent of a main shock as defined by the model.

shock as the largest earthquake within a sequence. Aftershocks are all the events occurring after the main shock within the same seismic sequence, while foreshocks are all the events that occur before the main shock, provided that they belong to the same sequence. Specifically, our analysis will focus on large main shocks, events that are sufficiently large to rupture the entire seismogenic thickness of the fault, or equivalently, those with a fractured area $A > Ly^2$. In real-world terms, if we assume a typical seismogenic thickness of $10 - 20$ km, empirical scaling laws (Wells & Coppersmith 1994; Strasser *et al.* 2010) suggest that such events correspond approximately to earthquakes of magnitude $M6.0 - 6.6$, providing a rough equivalence between our simulation results and natural seismicity. Given that the fault geometry is assumed to be rectangular, this rupture spans the full depth of the fault, clearly delineating the main shock within the seismic sequence. Aftershocks and foreshocks occur post- and pre-main shock, respectively.

An earthquake event is modelled as a series of slips that begin from an initial block instability; these slips define the epicentral coordinates. The seismic moment M_k released during the k-th earthquake is expressed as $M_k \propto \sum_i n_k(i)\Delta h$, where $n_k(i)$ counts the slips by the i-th block. The moment magnitude, m_k, is calculated using $m_k = (2/3)\log_{10}(M_k)$, assuming the constant of proportionality is zero for simplification.

The study simulates 100 000 main shocks to analyse patterns. We define the fractured area A_k for a main shock k as the number of lattice sites that slipped at least once during the event. The overlap λ between subsequent main shock areas A_k and A_{k+1} is quantified as:

$$\lambda = \frac{(A_{k+1} \cap A_k)}{\min(A_{k+1}, A_k)}. \qquad (2)$$

This metric reflects the spatial interaction between consecutive earthquakes, where $\lambda = 1$ indicates complete overlap and $\lambda = 0$ signifies no overlap.

5 RESULTS

5.1 Main shocks nucleation position

In this section we focus on main shocks only, neglecting aftershocks and foreshocks. In particular, we try to understand how the epicentre of a new main shock $(k + 1)$ is positioned relative to its predecessor (k). We specifically investigate the 1-D distance between these epicentres, defined $d_x^{\text{epi}} = |x_k^{\text{epi}} - x_{k+1}^{\text{epi}}|$. Given that our model has a fault size of $L_x = 10\,000$ and $L_y = 200$, yielding an aspect ratio of $L_y/L_x = 0.02$, depth variations are negligible compared to the lateral extent of the fault. As a result, we use epicentral distance rather than hypocentral distance, as it simplifies the interpretation without significantly altering the statistical properties of the results. This choice is further justified by the fact that main shocks in our model rupture the entire vertical seismogenic thickness (L_y), meaning that a 2-D spatial analysis would not provide additional insight but would instead introduce unnecessary complexity.

We indicate with $n_E(d_x^{\text{epi}})$ the number of main shock occurring at a distance d_x^{epi} from the previous one and with $n_{\text{tot}} = 100\,000$ the total main shock number. Fig. 3 displays the ratio of main shocks n_E/n_{tot}, that is, the fraction of the main shocks, as a function of d_x^{epi}. We also plot the theoretical distribution obtained in the case that the next earthquake occurs in a random position of the fault uncorrelated to the previous one. Fig. 3 shows that there is an excess of main shocks occurring at short distances d_x^{epi} from the previous main shock compared with the random ansatz. In particular, the distribution n_E presents a peak which roughly coincides with the characteristic size of the main shock, marked by a red dotted line. The distribution of the horizontal rupture length for several main shocks is shown in the Appendix A3. In our model, this characteristic size represents the typical maximum extent of rupture, which is inherently constrained by the system geometry and boundary conditions. Specifically the rupture propagates until it reaches the seismogenic thickness L_y, beyond which further growth is suppressed due to energy dissipation

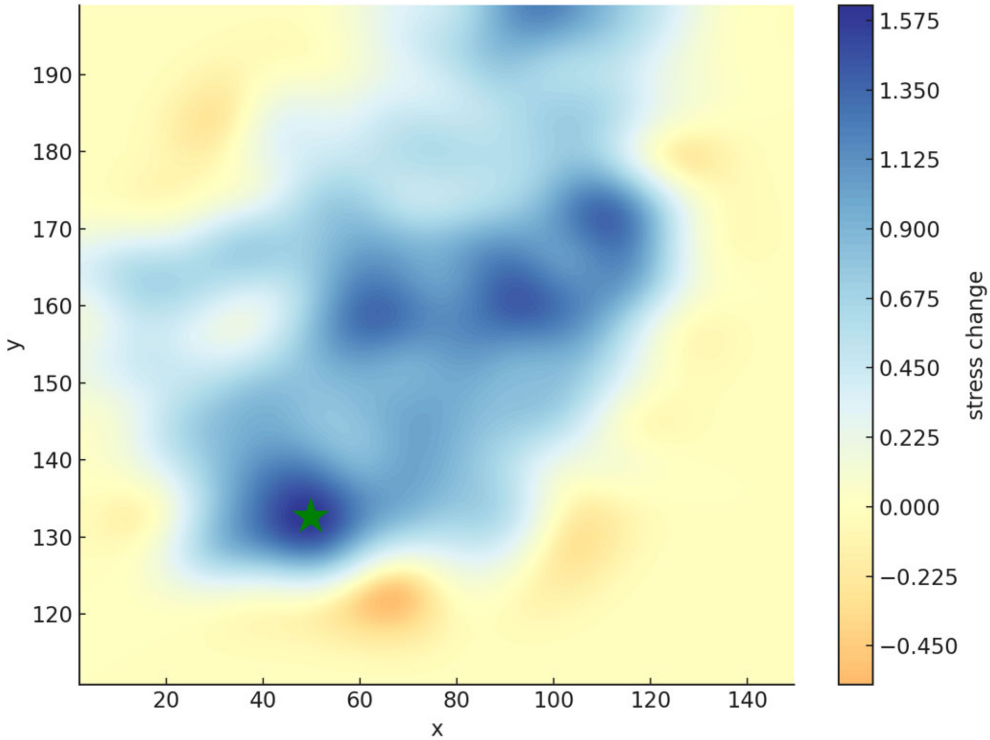

Figure 4. Map of stress change following an earthquake. The green star represents the epicentre location. The slipped region shows a significant stress drop, indicating areas unlikely to be reactivated in the near future. Conversely, zones surrounding the rupture exhibit localized stress increases (red areas), highlighting potential sites for future seismic activity.

at the boundaries. While this does not imply that all main shocks have exactly the same size, it establishes a natural upper bound on rupture growth, leading to the observed peak in the distribution. The accumulation of epicentre distances around this characteristic size suggests that new main shocks tend to nucleate near the peripheries of the rupture zones created by preceding shocks, indicating a spatial memory effect within the fault dynamics. As shown in the stress map following an earthquake (see Fig. 4), the entire region that has slipped is brought to a lower stress level and is unlikely to be reactivated afterwards. However, in the areas surrounding the slipped region, stress tends to concentrate in specific zones and it is in these areas that the probability of a subsequent main shock becomes higher.

To confirm the interpretation that two consecutive main shocks tend to occur close to each others we focus on the overlap between the fractured areas, A_k and A_{k+1}, from two consecutive events. More precisely, we evaluate the overlap using probabilities $P_{\mathrm{OFCR}}(\lambda)$ and $P_{\mathrm{RPM}}(\lambda)$, which measure the probability to observe an certain fraction overlap λ, under the numerical model and a random placement model (RPM), respectively. In particular, in the RPM, we simulate the dynamics of the same earthquake simulator but replace the x-coordinate of the second main shock identified with a random position along the fault. The histogram differences presented in Fig. 5 quantify the overlap between the fractured areas of consecutive main shocks. Since $P_{\mathrm{OFCR}} - P_{\mathrm{RPM}} > 0$ for $\lambda < 0.2$, the results indicate that subsequent events are more likely to nucleate near the peripheries of the rupture zone created by the previous main shock. This pattern suggests that the zones closest to the most recently activated fault segment—those under the greatest stress—are more prone to experience the next rupture. This observation supports the hypothesis that stress accumulation and release are localized phenomena within the fault zone (Turcotte 1977; Wetzler *et al.* 2018; Spassiani & Marzocchi 2021; Rafie *et al.* 2023). To test whether a similar spatial clustering is also observed in global seismicity, we analysed interevent distances for large earthquakes ($M_w \geq 6.5$) in the GCMT catalogue. The results reveal an excess of pairs at short distances compared to a randomized catalogue, suggesting that even at the global scale, large earthquakes preferentially occur near previous ruptures (see Appendix A4).

In the following we will provide support to the scenario where the subsequent main shock nucleates close to the boundaries of the previous main shock but the fracture mostly propagates in a region not involved by the previous slip. More precisely, we expect a situation pictorially represented in Fig. 6 where the epicentre of the subsequent main shock is closer to the previous main shock border compared to the other points involved in the subsequent main shock fracture.

To quantify this spatial relationship, we introduce an asymmetry factor, γ, defined as:

$$\gamma = \frac{|x_{k+1}^{\mathrm{epi}} - x_{k+1\to k}^{B}|}{\Delta x_{k+1}}, \tag{3}$$

where:

- x_{k+1}^{epi} is the epicentre of the main shock $k+1$,
- $x_{k+1\to k}^{B}$ is the boundary coordinate of the rupture zone of main shock $k+1$ that is closest to the epicentre of main shock k,
- $\Delta x_{k+1} = \max(x_{k+1}) - \min(x_{k+1})$ represents the length of the rupture zone of main shock $k+1$.

The asymmetry factor γ helps determine whether the epicentre of a new main shock $k+1$ is positioned near or far from the area influenced by the previous main shock k. A γ value close to 0 indicates that the epicentre of main shock $k+1$ is near the boundary of the rupture zone of main shock k, suggesting a higher likelihood

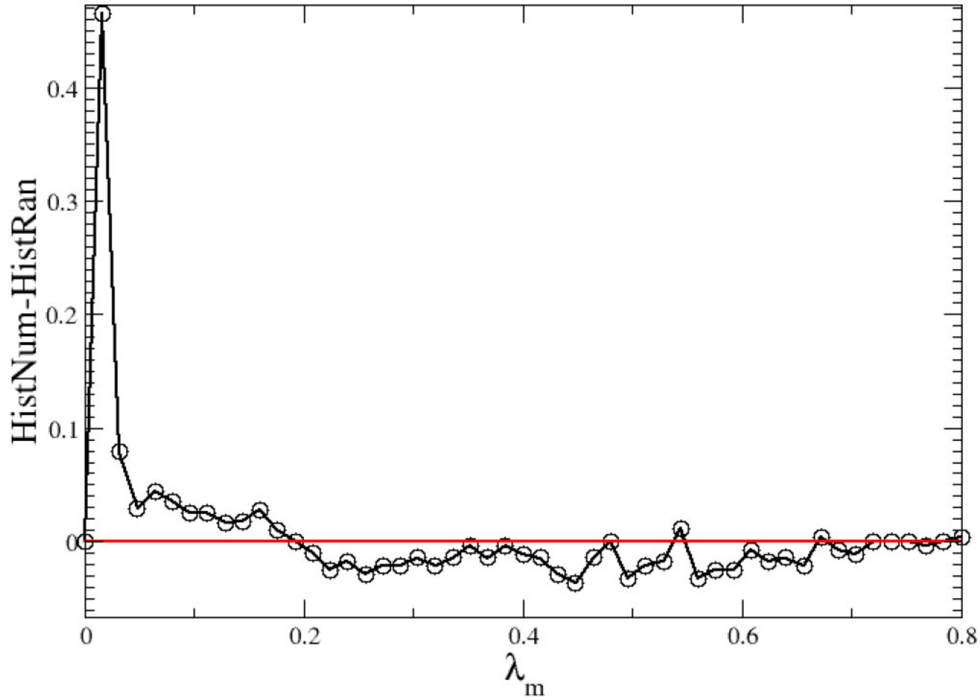

Figure 5. Differences in the overlap histograms $P_{\mathrm{OFCR}}(\lambda) - P_{\mathrm{ran}}(\lambda)$ for two consecutive main shocks, where λ quantifies the fraction of overlap. The null hypothesis represented by the horizontal red line assumes random overlaps.

of being influenced by the residual stress or weakened fault structure left by main shock k. Conversely, a γ value close to 1 means that the epicentre is near the opposite boundary, indicating nucleation in an area less affected by the previous main shock's stress shadow.

The analysis of γ across many seismic events provides insights into the typical behaviour of fault reactivation. As shown in Fig. 7, the distribution of γ values indicates that subsequent main shock epicentres are more likely to occur near the peripheries of the last event's rupture zone. This is attributed to the stress concentrations that build up along the edges of a ruptured fault segment. The higher probability of observing lower γ values (indicating proximity to the previous rupture) confirms the hypothesis that areas near a recent rupture are more likely to fail due to increased stress and existing fault weaknesses.

Our results may seem to differ from instrumental data suggesting no preferential triggering of earthquakes in regions of increased static stress (Kagan & Jackson 1998; Huc & Main 2003). However, this apparent difference likely arises from two key aspects of our model that are not included in standard static stress analyses: threshold heterogeneity and stress relaxation.

Introducing heterogeneity implies that even small stress perturbations can trigger instabilities in areas already near failure. Moreover, afterslip-induced stress redistribution gradually alters the static stress field, so that subsequent triggering is driven more by the relaxation process than by the initial stress increase. These features are consistently reproduced in our simulations and, in our view, could offer valuable insights into the underlying dynamics of real-world seismic activity.

5.2 The magnitude distribution of aftershocks and foreshocks

Numerical simulations offer also a detailed insight for examining the relationship between aftershock magnitudes and their spatial distance to the main shock and how stress fields are modified following a seismic event.

In the hypothesis that magnitudes obey the Gutenberg–Richter law, $P(m) \sim 10^{-bm}$, the coefficient b can be obtained by maximum-likelihood estimation (Aki 1965)

$$b_{\mathrm{th}} = \frac{1}{\langle m \rangle - m_{\mathrm{th}}}, \tag{4}$$

where $\langle m \rangle$ is the average magnitude of earthquakes with magnitudes larger than a lower threshold m_{th}. When $P(m)$ is a pure exponential decay, $b_{\mathrm{th}} = b$, but this is no longer true when deviations from exponential decay are present. In particular, the presence of truncation at large magnitudes strongly affects b_{th}.

In laboratory experiments (Amitrano 2003), it has been demonstrated that b_{th} can act as a stress metre (e.g. Tormann *et al.* 2014), and many studies monitor its evolution in time and space in instrumental catalogues (Godano & Petrillo 2023; Godano *et al.* 2024a, b). Recently, to avoid biases related to the incompleteness of instrumental data sets, it is preferred to focus on eq. (4) by replacing $\langle m \rangle$ with the average magnitude of positive magnitude differences (van der Elst 2021; Lippiello & Petrillo 2024). In numerical studies, there are no problems of incompleteness, and we can use the traditional estimate (eq. 4) using a lower magnitude threshold $m_{\mathrm{th}} = 0.5$.

As shown in Fig. 8, the magnitude distribution of aftershocks presents different slopes if we restrict to aftershocks with overlap larger or smaller than $\lambda_A = 0.5$. Here λ_A represents the same quantity λ defined in eq. (2) but considering the second event area A_{k+1} as the area of the aftershock linked to the main shock k. Namely

$$\lambda_A = \frac{(A_{k'} \cap A_k)}{\min(A_{k'}, A_k)}, \tag{5}$$

where k' is the index of the aftershock related to the main shock k. We find that b_{th} decreases with λ_A (Fig. 8c). Conversely, a similar

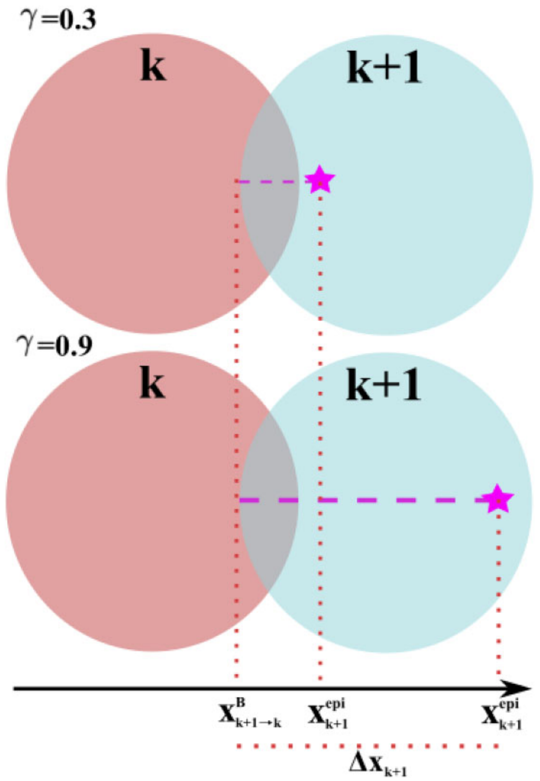

Figure 6. Illustration of the asymmetry factor γ, demonstrating how the epicentre of main shock $k+1$ (x^{epi}_{k+1}) is measured relative to the closest boundary ($x^{B}_{k+1\to k}$) of the previous main shock rupture zone. The circles represent a qualitative schematic representation of rupture areas to facilitate visualization and the definition of key quantities. In reality, the earthquake simulator produces irregular rupture shapes rather than perfect circles. As an example, the upper case, $\gamma = 0.3$, indicates that rupture zone of the $k+1$-event is influenced by the residual stress of the main shock k. Conversely, the lower case $\gamma = 0.9$ indicates that the nucleation occurs far from the previous main shock's stress shadow.

pattern is not observed when considering foreshocks (Fig. 8b), that is, when b_{th} remains basically unchanged for each overlap value λ_A.

In our understanding the dependence on λ_A from the average magnitude of aftershocks is mostly caused by the existence of a maximum observed magnitude which depends on λ_A. This is already evident from Fig. 8 by the comparison of the magnitude distributions with λ_A smaller or larger than 0.5 but it is better enlightened in Fig. 9 where we plot the maximum observed magnitude, $m_{\max}$, for aftershocks as a function of λ_A. More precisely, we estimate this quantity via the maximum area by considering the ratio $\Sigma_A = \langle A^2\rangle/\langle A\rangle$ which if A follows a power law in the range $[1, A_{\max}]$ is proportional to $A_{\max}$.

The quantity Σ_A represents the mean square to mean ratio of the aftershock (or foreshock) area. This quantity offers more statistically robust picture of seismic activity by highlighting the variability and typical magnitudes of events within a given data set respect to calculate directly the maximum value of the area.

Our simulations demonstrate a clear dependence of aftershock magnitudes on their proximity to the main shock rupture zone. Panel (a) of Fig. 9 illustrates the relationship between the aftershocks Σ_A and the overlap, λ_A, with the main shock. This is consistent with the hypothesis that the release of seismic energy during the main shock leads to a significant drop in residual stress levels, thereby limiting the energy available for subsequent aftershocks within this zone. Conversely, areas outside the immediate rupture zone of the main shock, which experience less stress release, are capable of hosting larger aftershocks. This pattern suggests a spatial variation in stress accumulation and release, where the edges of the rupture zone, still under considerable stress, are likely sites for stronger aftershocks.

Foreshock behaviour deserves special attention, as it sits at the centre of a long-standing debate. Two main interpretations exist. In the bottom-up triggering scenario (Mignan 2014), foreshocks arise from standard cascading triggering processes—with the key assumption that a smaller event can trigger a larger one. Under this view, foreshock–main shock pairs represent rare statistical fluctuations within the more common main shock–aftershock dynamics. Consequently, foreshocks are not considered reliable precursors of large earthquakes. This perspective is supported by several studies (Helmstetter *et al.* 2003; Helmstetter & Sornette 2003; Felzer *et al.* 2004; Marzocchi & Zhuang 2011).

In contrast, the top-down loading model (Mignan 2014) sees foreshocks as passive indicators of a larger scale tectonic preparation process—such as aseismic slip gradually loading the fault prior to a main shock. In this view, foreshocks are distinct from typical aftershocks and may offer predictive insight into impending large events. This interpretation is supported by a growing body of research (Lippiello *et al.* 2012; Shearer 2012; Ogata & Katsura 2014; de Arcangelis *et al.* 2016; Seif *et al.* 2019; Trugman & Ross 2019; Petrillo & Lippiello 2021, 2023).

In our simulations, foreshocks display a markedly different behaviour from aftershocks. Specifically, we observe no significant correlation between foreshock locations and the future rupture area of the main shock (Fig. 9, panel b), in contrast with aftershocks, which cluster where stress has been redistributed. This suggests that foreshocks may be governed by slow and spatially distributed stress accumulation rather than by localized stress interactions. Overall, our findings align more closely with the top-down loading hypothesis, though they do not definitively resolve this complex and highly debated issue.

5.3 Analysis of interevent distances in the GCMT catalogue

To assess whether the spatial clustering of large earthquakes identified in our model also manifests in real seismicity, we analysed the global GCMT catalogue from 1976 to 2020, focusing on events with moment magnitude $M_w \geq 6.0$. For this analysis, we computed the pairwise epicentral distances between earthquakes in the catalogue, considering only distances less than or equal to 2000 km to restrict the study to regional scales where interactions between large ruptures are plausible.

Given a catalogue of N earthquakes, we considered all possible pairs of events (i, j), with $j = i + 1$ and computed the great-circle distance d_{ij} between their epicentres using the geodesic distance on the Earth surface. The set of distances d_{ij} was then used to estimate the probability density function $P_{\text{CMT}}(d)$ of interevent distances.

To evaluate whether the observed spatial distribution deviates from randomness, we generated a synthetic catalogue by extracting randomly one of the two events from the GCMT catalogue. We repeated this procedure multiple times to generate bootstrap ensembles of random catalogues, from which we computed the corresponding mean PDF $\tilde{P}_{\text{rand}}(d)$ and its standard deviation $\sigma_{\text{rand}}(d)$.

The comparison between real and random catalogues is quantified by the difference:

$$\Delta P(d) = \tilde{P}_{\text{CMT}}(d) - \tilde{P}_{\text{rand}}(d), \tag{6}$$

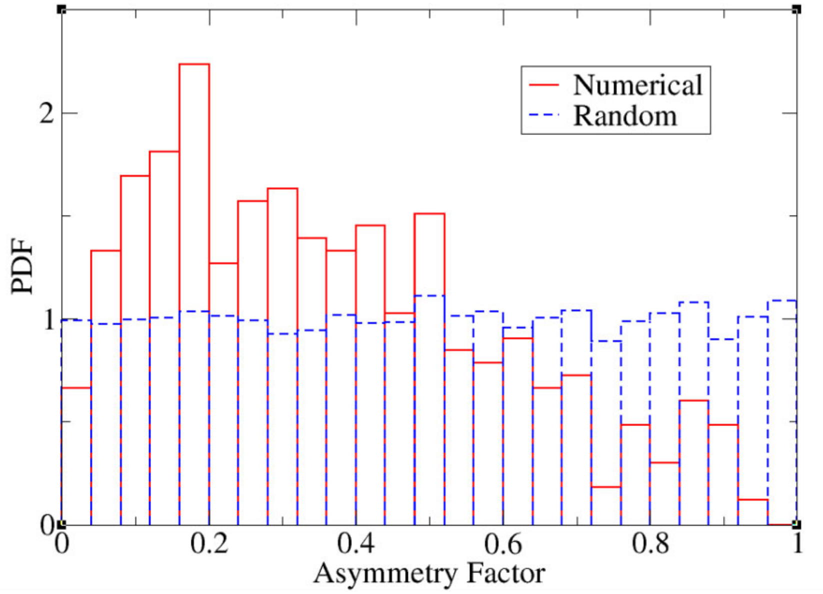

Figure 7. Probability density function (PDF) of the asymmetry factor γ for 100 000 main shocks, with the red histogram representing the OFCR model and the dashed blue histogram representing a uniform distribution as a null hypothesis. This figure highlights the prevalence of asymmetric nucleation sites in subsequent main shocks, suggesting a tendency for new earthquakes to initiate close to the boundaries of previous ruptures.

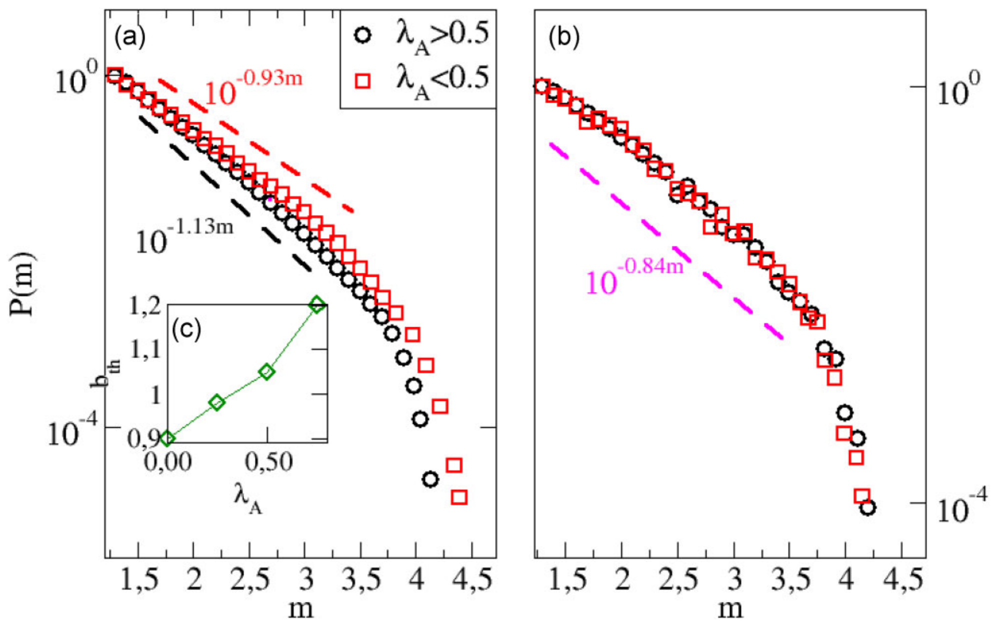

Figure 8. The magnitude distribution $P(m)$ calculated for the aftershocks (panel a) and for foreshocks (panel b). Black circles indicate the magnitude distribution calculated only for the events characterized by $\lambda_A > 0.5$, while red squares those characterized by events with $\lambda_A < 0.5$. (c) The quantity $b_{\rm th}$ (eq. 4) as a function of the overlap, λ_A, between aftershocks and the related main shock.

with associated uncertainty estimated as:

$$\sigma_\Delta(d) = \sqrt{\sigma_{\rm CMT}(d)^2 + \sigma_{\rm rand}(d)^2}, \quad (7)$$

where $\sigma_{\rm CMT}(d)$ is the standard deviation of the PDF estimated via bootstrap resampling of the real catalogue. Fig. 10 shows the function $\Delta P(d)$, representing the excess probability of earthquake pairs as a function of epicentral distance d. The plot reveals a clear positive excess at short distances, particularly between approximately 10 km and 100 km—a range that corresponds to the typical rupture lengths of earthquakes with magnitudes between M_w 6 and 7, which dominate the data set. This suggests that large earthquakes tend to occur preferentially near previous large ruptures, deviating from what would be expected under a random spatial distribution.

At very short distances ($d < 10$ km), the excess vanishes, likely due to limitations in the spatial resolution of earthquake locations and inherent uncertainties in centroid determinations within the GCMT catalogue. Conversely, at larger distances, $\Delta P(d)$ becomes negative, effectively compensating for the excess at shorter scales, as the integral of $\Delta P(d)$ over all distances must sum to zero by construction.

These results indicate that, even on a global scale, the spatial distribution of large earthquakes is not entirely random. Instead, they exhibit clustering at characteristic distances comparable to their

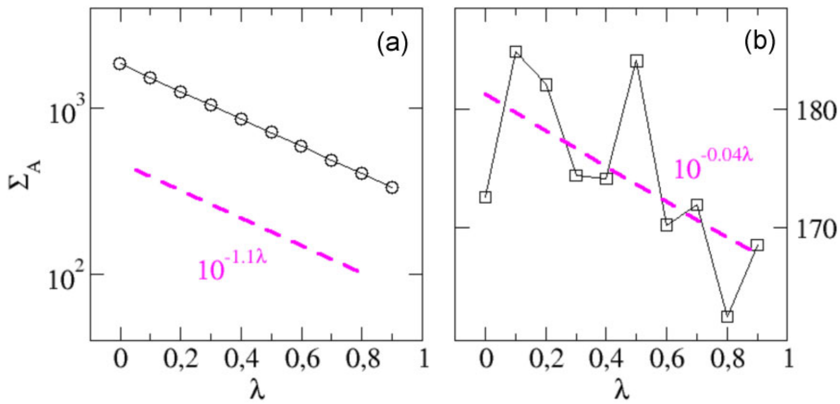

Figure 9. The Σ_A as a function of the overlap λ_A, between the aftershock and the main shock panel (a) and between the foreshocks and the main shock (panel b).

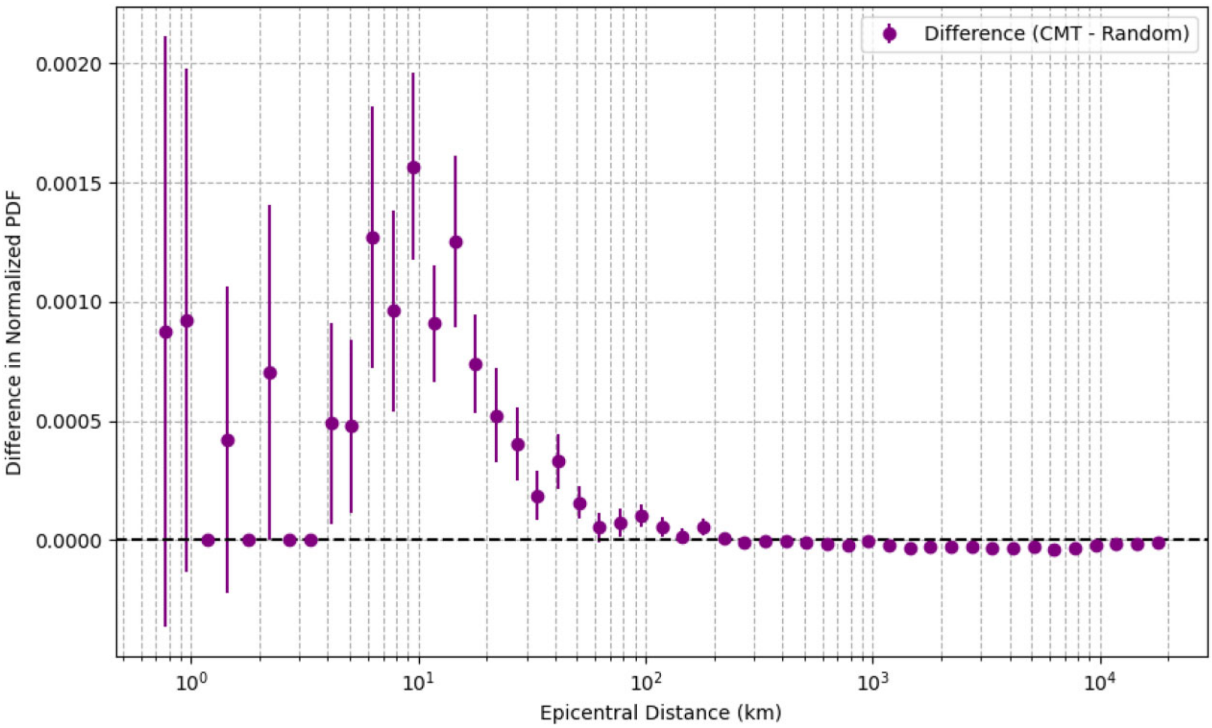

Figure 10. Difference between the normalized interevent distance PDFs of the real GCMT catalogue ($M_w \geq 6.0$) and randomized catalogues. The curve shows the excess probability density of finding earthquake pairs at a given distance in the real catalogue compared to a spatially random distribution. Error bars indicate one standard deviation estimated from bootstrap resampling. The positive peak at short distances highlights a significant clustering of large earthquakes within $10 - 100$ km.

rupture lengths. This observation is consistent with the mechanisms embedded in our model, where stress concentration around recent rupture zones promotes the occurrence of subsequent large events.

6 CONCLUSIONS

This study has shown how earthquake simulators can explain some important empirical features, providing a physical background to them, and, at the same time, they can stimulate the search of new empirical patterns. Our simulations reveal that the location of main shocks significantly influences the location the next big event, which preferentially occurs on the high stressed regions near the boundary of the previous main shock. This information can be very useful for improving existing earthquake forecasting models, such as the ETAS model, which assumes that the magnitude of subsequent shocks is not altered by the previous seismicity. Incorporating observed mechanisms of stress accumulation and redistribution into these models could lead to significant improvements in the spatial forecasting of large earthquakes.

Our study also shows that the magnitude–frequency distribution of aftershocks is strongly affected by the stress redistributed by the main shock, inhibiting the nucleation of large earthquakes inside the part of fault that has just slipped. In particular, we have established a quantitative relationship between the magnitude of aftershocks and their spatial overlap with the main shock of the same sequence. Conversely, similar patterns are not observed when considering the statistical features of foreshocks.

While our model successfully reproduces key statistical features of earthquake sequences, it does not account for several complexities present in real seismicity. In natural earthquake sequences, spatiotemporal variations in frictional properties, and complex fault geometries could influence stress redistribution and aftershock triggering. Additionally, the assumption that large main shocks rupture through the entire seismogenic thickness may not always hold, especially for smaller events, potentially affecting aftershock location patterns. In a future work, relaxing some of this assumption could provide further insights into the mechanisms governing earthquake interactions.

These insights could be particularly valuable in regions prone to seismic activity, helping scientists improve the accuracy and reliability of earthquake forecasting models.

ACKNOWLEDGMENTS

JZ acknowledges support by MEXT Project for Seismology TowArd Research innovation with Data of Earthquake (STAR-E Project), Grant Number: JPJ010217. EL acknowledges support from project PRIN201798CZLJ and from VALERE project of the University of Campania "L. Vanvitelli". WM has been partially supported by the RETURN Extended Partnership and received funding from the European Union Next-GenerationEU (National Recovery and Resilience Plan–NRRP, Mission 4, Component 2, Investment 1.3–D.D. 1243 2/8/2022, PE0000005). G.P. would like to acknowledge the Earth Observatory of Singapore (EOS), and the Singapore Ministry of Education Tier 3b project "Investigating Volcano and Earthquake Science and Technology (InVEST)

AUTHOR CONTRIBUTIONS

Conceptualization: EL, GP, WM, Data curation: GP, Formal analysis: GP, Funding acquisition: WM, Investigation: GP, EL, WM Methodology: EL, WM, Project Administration: n/a, Resources: n/a, Software: GP, EL Supervision: GP, EL, WM, JZ Validation: GP, EL, WM Writing–original draft: GP, EL, WM Writing–review and editing: GP, EL, WM, JZ.

DATA AVAILABILITY

The data underlying this article will be shared on reasonable request to the corresponding author.

REFERENCES

Aki, K., 1965. Maximum likelihood estimate of b in the formula $\log n = a - bm$ and its confidence limits, *Bull. Earthq. Res. Inst., Univ. Tokyo,* **43,** 237–239.

Amitrano, D., 2003. Brittle-ductile transition and associated seismicity: Experimental and numerical studies and relationship with the b value, *J. geophys. Res.: Solid Earth,* **108**(B1).

Bak, P. & Tang, C., 1989. Earthquakes as a self-organized critical phenomenon, *J. geophys. Res.: Solid Earth,* **94**(B11), 15635–15637.

Burridge, R. & Knopoff, L., 1967. Model and theoretical seismicity, *Bull. seism. Soc. Am.,* **57**(3), 341–371.

Console, R., Jackson, D. & Kagan, Y., 2010. Using the etas model for catalog declustering and seismic background assessment, *Pure appl. Geophys.,* **167,** 819–830.

de Arcangelis, L., Godano, C., Grasso, J.R. & Lippiello, E., 2016. Statistical physics approach to earthquake occurrence and forecasting, *Phys. Rep.,* **628,** 1–91.

Duputel, Z., Agram, P.S., Simons, M., Minson, S.E. & Beck, J.L., 2014. Accounting for prediction uncertainty when inferring subsurface fault slip, *Geophys. J. Int.,* **197**(1), 464–482.

Felzer, K.R., Abercrombie, R.E. & Ekstrom, G., 2004. A common origin for aftershocks, foreshocks, and multiplets, *Bull. seism. Soc. Am.,* **94**(1), 88–98.

Godano, C. & Petrillo, G., 2023. Estimating the completeness magnitude m_c and the b-values in a snap, *Earth Space Sci.,* **10**(2). doi: 10.1029/2022EA002540.

Godano, C., Petrillo, G. & Lippiello, E., 2024a. Evaluating the incompleteness magnitude using an unbiased estimate of the b value, *Geophys. J. Int.,* **236**(2), 994–1001.

Godano, C., Tramelli, A., Petrillo, G. & Convertito, V., 2024b. Testing the predictive power of b value for Italian seismicity, *Seismica,* **3**(1).

Hainzl, S., Zöller, G. & Kurths, J., 1999. Similar power laws for foreshock and aftershock sequences in a spring-block model for earthquakes, *J. geophys. Res.: Solid Earth,* **104**(B4), 7243–7253.

Helmstetter, A. & Sornette, D., 2003. Foreshocks explained by cascades of triggered seismicity, *J. geophys. Res.: Solid Earth,* **108**(B10).

Helmstetter, A., Sornette, D. & Grasso, J.-R., 2003. Main shocks are aftershocks of conditional foreshocks: How do foreshock statistical properties emerge from aftershock laws, *J. geophys. Res.: Solid Earth,* **108**(B1).

Huc, M. & Main, I.G., 2003. Anomalous stress diffusion in earthquake triggering: Correlation length, time dependence, and directionality, *J. geophys. Res.: Solid Earth,* **108**(B7).

Jagla, E., 2011. Delayed dynamic triggering of earthquakes: Evidence from a statistical model of seismicity, *Europhys. Lett.,* **93**(1), 19001.

Jagla, E. & Kolton, A., 2010. A mechanism for spatial and temporal earthquake clustering, *J. geophys. Res.: Solid Earth,* **115**(B5).

Jagla, E.A., 2010. Realistic spatial and temporal earthquake distributions in a modified Olami-Feder-Christensen model, *Phys. Rev. E—Statistical, Nonlinear, and Soft Matter Physics,* **81**(4), 046117.

Jagla, E.A., 2013. Forest-fire analogy to explain the b value of the Gutenberg-Richter law for earthquakes, *Phys. Rev. Lett.,* **111**(23), 238501.

Jagla, E.A., 2014. Aftershock production rate of driven viscoelastic interfaces, *Phys. Rev. E,* **90**(4), 042129.

Jagla, E.A., Landes, F.P. & Rosso, A., 2014. Viscoelastic effects in avalanche dynamics: a key to earthquake statistics, *Phys. Rev. Lett.,* **112**(17), 174301.

Kagan, Y.Y. & Jackson, D.D., 1998. Spatial aftershock distribution: effect of normal stress, *J. geophys. Res.: Solid Earth,* **103**(B10), 24453–24467.

Landes, F.P. & Lippiello, E., 2016. Scaling laws in earthquake occurrence: disorder, viscosity, and finite size effects in Olami-Feder-Christensen models, *Phys. Rev. E,* **93**(5), 051001.

Landes, F.P., Rosso, A. & Jagla, E.A., 2015. Frictional dynamics of viscoelastic solids driven on a rough surface, *Phys. Rev. E,* **92**(1), 012407.

Li, Y., Zhao, D., Shan, X., Gao, Z., Huang, X. & Gong, W., 2022. Coseismic slip model of the 2022 M_w 6.7 Luding (Tibet) earthquake: Pre- and post-earthquake interactions with surrounding major faults, *Geophys. Res. Lett.,* **49**(24), e2022GL102043.

Lippiello, E. & Petrillo, G., 2024. b-more-incomplete and b-more-positive: Insights on a robust estimator of magnitude distribution, *J. geophys. Res.: Solid Earth,* **129**(2), e2023JB027849.

Lippiello, E., Marzocchi, W., de Arcangelis, L. & Godano, C., 2012. Spatial organization of foreshocks as a tool to forecast large earthquakes, *Sci. Rep.,* **2**(1), 846.

Lippiello, E., Giacco, F., Marzocchi, W., Godano, C. & de Arcangelis, L., 2015. Mechanical origin of aftershocks, *Sci. Rep.,* **5**(1), 15560.

Lippiello, E., Petrillo, G., Landes, F. & Rosso, A., 2019. Fault heterogeneity and the connection between aftershocks and afterslip, *Bull. seism. Soc. Am.,* **109**(3), 1156–1163.

Lippiello, E., Petrillo, G., Landes, F. & Rosso, A., 2021. The genesis of aftershocks in spring slider models, *Stat. Methods Model. Seismogenesis,* **1,** 131–151.

Lombardi, A.M. & Marzocchi, W., 2010. The etas model for daily forecasting of italian seismicity in the csep experiment, *Ann. Geophys.,* **53**. doi: 10.4401/ag-4848.

Marzocchi, W. & Zhuang, J., 2011. Statistics between main shocks and foreshocks in italy and southern California, *Geophys. Res. Lett.,* **38**(9).

Mignan, A., 2014. The debate on the prognostic value of earthquake foreshocks: a meta-analysis, *Sci. Rep.,* **4**(1), 4099.

Mori, T. & Kawamura, H., 2008. Spatiotemporal correlations of earthquakes in the continuum limit of the one-dimensional Burridge-Knopoff model, *J. geophys. Res.: Solid Earth,* **113**(B11).

Nakanishi, H., 1992. Earthquake dynamics driven by a viscous fluid, *Phys. Rev. A,* **46**(8), 4689.

Naylor, M. & Main, I., 2008. Cell scale self-organisation in the OFC model for earthquake dynamics, *Eur. Phys. J. B: Condensed Matter and Complex Systems,* **64**(1), 139–146.

Ogata, Y., 1988. Statistical models for earthquake occurrences and residual analysis for point processes, *J. Am. Stat. Assoc.,* **83**(401), 9–27.

Ogata, Y. & Katsura, K., 2014. Comparing foreshock characteristics and foreshock forecasting in observed and simulated earthquake catalogs, *J. geophys. Res.: Solid Earth,* **119**(11), 8457–8477.

Ohno, K., Ohta, Y., Hino, R., Koshimura, S., Musa, A., Abe, T. & Kobayashi, H., 2022. Rapid and quantitative uncertainty estimation of coseismic slip distribution for large interplate earthquakes using real-time GNSS data and its application to tsunami inundation prediction, *Earth Planets Space,* **74,** 24.

Olami, Z., Feder, H. J. S. & Christensen, K., 1992. Self-organized criticality in a continuous, nonconservative cellular automaton modeling earthquakes, *Phys. Rev. Lett.,* **68**(8), 1244.

Perfettini, H. & Avouac, J.-P., 2004. Postseismic relaxation driven by brittle creep: a possible mechanism to reconcile geodetic measurements and the decay rate of aftershocks, application to the chi-chi earthquake, taiwan, *J. geophys. Res.: Solid Earth,* **109**(B2).

Petrillo, G. & Lippiello, E., 2021. Testing of the foreshock hypothesis within an epidemic like description of seismicity, *Geophys. J. Int.,* **225**(2), 1236–1257.

Petrillo, G. & Lippiello, E., 2023. Incorporating foreshocks in an epidemic-like description of seismic occurrence in italy, *Appl. Sci.,* **13**(8).

Petrillo, G. & Zhuang, J., 2024. Bayesian earthquake forecasting approach based on the epidemic type aftershock sequence model, *Earth Planets Space,* **76**(1), 78.

Petrillo, G., Lippiello, E., Landes, F.P. & Rosso, A., 2020. The influence of the brittle-ductile transition zone on aftershock and foreshock occurrence, *Nature Commun.,* **11**(1), 3010.

Petrillo, G., Rosso, A. & Lippiello, E., 2022. Testing of the seismic gap hypothesis in a model with realistic earthquake statistics, *J. geophys. Res.: Solid Earth,* **127**(6).

Petrillo, G., Lippiello, E. & Zhuang, J., 2024. Including stress relaxation in point-process model for seismic occurrence, *Geophys. J. Int.,* **236**(3), 1332–1341.

Rafie, M., Sahara, D., Cummins, P., Triyoso, W. & Widiyantoro, S., 2023. Stress accumulation and earthquake activity on the Great Sumatran Fault, Indonesia, *Nat. Hazards,* **116**.

Ross, G.J., 2021. Bayesian estimation of the ETAS model for earthquake occurrences, *Bull. seism. Soc. Am.,* **111**(3), 1473–1480.

Ross, G.J. & Kolev, A.A., 2022. Semiparametric Bayesian forecasting of SpatioTemporal earthquake occurrences, *Ann. Appl. Stat.,* **16**(4), 2083–2100.

Schoenberg, F. & Bolt, B., 2000. Short-term exciting, long-term correcting models for earthquake catalogs, *Bull. seism. Soc. Am.,* **90**(4), 849–858.

Seif, S., Zechar, J.D., Mignan, A., Nandan, S. & Wiemer, S., 2019. Foreshocks and their potential deviation from general seismicity, *Bull. seism. Soc. Am.,* **109**(1), 1–18.

Shearer, P.M., 2012. Self-similar earthquake triggering, båth's law, and foreshock/aftershock magnitudes: Simulations, theory, and results for southern California, *J. geophys. Res.: Solid Earth,* **117**(B6).

Spassiani, I. & Marzocchi, W., 2021. An energy-dependent earthquake moment–frequency distribution, *Bull. seism. Soc. Am.,* **111**(2), 762–774.

Spassiani, I., Petrillo, G. & Zhuang, J., 2024. Distribution related to all samples and extreme events in the ETAS cluster, *Seismol. Res. Lett.,* **95,** 3234–3242. doi: 10.1785/0220230324.

Stallone, A. & Marzocchi, W., 2019. Features of seismic sequences are similar in different crustal tectonic regions, *Bull. seism. Soc. Am.,* **109**(5), 1594–1604.

Strasser, F.O., Arango, M. & Bommer, J.J., 2010. Scaling of the source dimensions of interface and intraslab subduction-zone earthquakes with moment magnitude, *Seismol. Res. Lett.,* **81**(6), 941–950.

Tormann, T., Wiemer, S. & Mignan, A., 2014. Systematic survey of high-resolution *b* value imaging along Californian faults: inference on asperities, *J. geophys. Res.: Solid Earth,* **119**(3), 2029–2054.

Touati, S., Naylor, M. & Main, I.G., 2009. Origin and nonuniversality of the earthquake interevent time distribution, *Phys. Rev. Lett.,* **102**(16), 168501.

Trugman, D.T. & Ross, Z.E., 2019. Pervasive foreshock activity across southern California, *Geophys. Res. Lett.,* **46**(15), 8772–8781.

Turcotte, D.L., 1977. Stress accumulation and release on the San Andreas fault, *PAGEOPH,* **115,** 413–427. doi: 10.1007/BF01637118.

Utsu, T., Ogata, Y., S, R. &, 1995. The centenary of the Omori formula for a decay law of aftershock activity, *J. Phys. Earth,* **43**(1), 1–33.

van der Elst, N.J., 2021. B-positive: a robust estimator of aftershock magnitude distribution in transiently incomplete catalogs, *J. geophys. Res.: Solid Earth,* **126**(2), e2020JB021027.

van der Elst, N.J. & Shaw, B.E., 2015. Larger aftershocks happen farther away: Nonseparability of magnitude and spatial distributions of aftershocks, *Geophys. Res. Lett.,* **42**(14), 5771–5778.

Wei, G., Chen, K., Lyu, M., Gong, W., Dal Zilio, L., Ye, L. & Tu, H., 2023. Complex strike-slip faulting during the 2021 M_w 7.4 Maduo earthquake, *Commun. Earth Environ.,* **4,** 1234567890. doi: 10.1038/s43247-023-00980-6.

Wells, D.L. & Coppersmith, K.J., 1994. New empirical relationships among magnitude, rupture length, rupture width, rupture area, and surface displacement, *Bull. seism. Soc. Am.,* **84**(4), 974–1002.

Wetzler, N., Lay, T., Brodsky, E.E. & Kanamori, H., 2018. Systematic deficiency of aftershocks in areas of high coseismic slip for large subduction zone earthquakes, *Sci. Adv.,* **4**(2), eaao3225.

Zheng, Y., Enescu, B., Zhuang, J. & Yu, C., 2021. Data replenishment of five moderate earthquake sequences in Japan, with semi-automatic cluster selection, *Earthq. Sci.,* **34**(4), 310–322.

Zhuang, J., 2012. Long-term earthquake forecasts based on the epidemic-type aftershock sequence (ETAS) model for short-term clustering, *Res. Geophys.,* **2**(1), e8–e8.

APPENDIX A: MODEL OUTPUTS

A1 Burn-in data

In Fig. A1 we show the catalogue produced by the earthquake simulator. The numerical catalogue generated by our model exhibits an initial transient phase, during which the characteristic event magnitudes increase before reaching a statistically stationary regime.

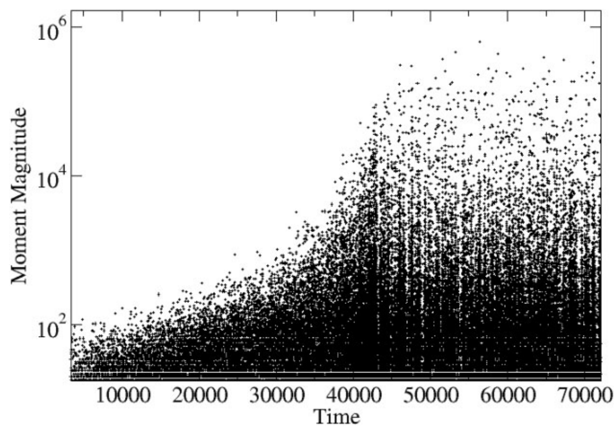

Figure A1. The seismic catalogue produced by the earthquake simulator. We show here the moment magnitude against the time.

This behaviour arises as the system gradually redistributes stress and adjusts from its initial conditions. In statistical physics, a similar process is often referred to as thermalization, where a system evolves towards a steady state through internal energy redistribution. To ensure that our analysis focuses on the fully developed seismicity, we discard the initial transient (burn-in) phase and consider only the catalogue corresponding to the stationary regime (in our case Time $> 50\,000$). This ensures that our results are not influenced by artefacts related to the initialization of the simulation but instead reflect the long-term statistical properties of the system.

A2 Mean stress analysis

In Fig. A2 we further characterize the stress dynamics in our model, we analysed the mean stress in the brittle layer before (green curves) and after (blue curves) the occurrence of a main shock. This was done by computing the mean stress over multiple main shock events in the simulation to obtain statistical distributions. The analysis is performed in four different spatial regions around the main shock epicentre. In particular within a radius $r = 10, 20, 30$ and across the entire fault system.

As shown in Fig. A2, the mean stress before a main shock is consistently higher than after the event, confirming that earthquakes result in a significant local stress drop. Furthermore, this stress drop is more pronounced when focusing on smaller regions around the epicentre (e.g. $r = 10$), while it becomes less evident when averaging over larger areas, including regions that were not directly involved in the rupture. This result is expected, as stress redistribution primarily affects the areas closest to the rupture zone.

A3 Distribution of the horizontal rupture length

To justify the choice of the vertical dashed red line in Fig. 3, we computed the probability density function (PDF) of the horizontal rupture length from our simulation. Fig. A3 presents the resulting distribution, showing the typical rupture lengths observed in our model.

The distribution exhibits a well-defined peak around 100, indicating a characteristic rupture size, with most events having a horizontal rupture length concentrated around this peak. The tail of the distribution suggests that larger ruptures are possible but occur with lower probability.

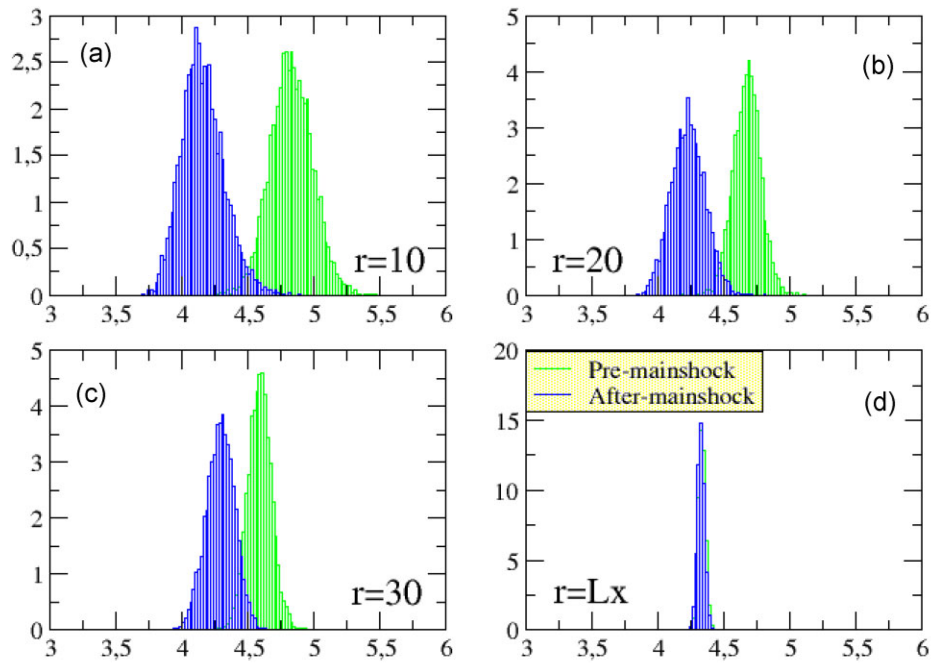

Figure A2. Mean stress distribution before and after main shocks, computed in different spatial regions. The distributions are obtained by averaging over multiple main shock events in the simulation. The stress is computed in four different spatial windows: (a) within a radius $r = 10$, (b) within $r = 20$, (c) within $r = 30$, and (d) over the entire fault system. In all cases, the mean stress before the main shock (green) is higher than the mean stress after the main shock (blue), reflecting the expected stress drop following a rupture. The difference between pre- and post-seismic stress is most pronounced for small radii, where stress redistribution is more localized, while it diminishes when averaging over the entire fault system.

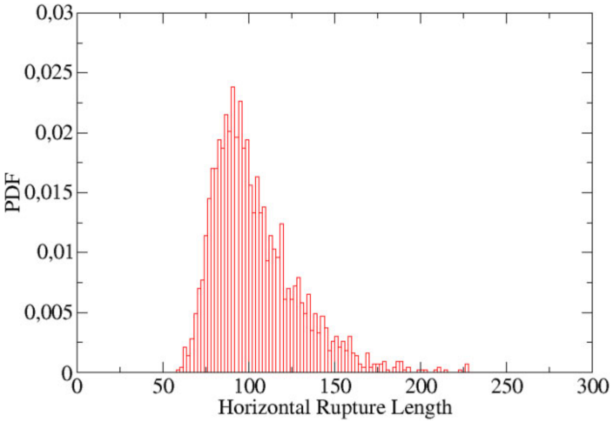

Figure A3. Probability density function (PDF) of the horizontal rupture length from the simulations. The distribution exhibits a well-defined peak around 100, indicating the most typical rupture size in the model.